LETTER

https://doi.org/10.1038/s41586-019-1481-z

Quantifying inactive lithium in lithium metal batteries

Chengcheng Fang[1,6], Jinxing Li[2,6], Minghao Zhang[2], Yihui Zhang[1], Fan Yang[3], Jungwoo Z. Lee[2], Min-Han Lee[1], Judith Alvarado[1,4], Marshall A. Schroeder[4], Yangyuchen Yang[1], Bingyu Lu[2], Nicholas Williams[3], Miguel Ceja[2], Li Yang[5], Mei Cai[5], Jing Gu[3], Kang Xu[4], Xuefeng Wang[2] & Ying Shirley Meng[1,2]*

Lithium metal anodes offer high theoretical capacities (3,860 milliampere-hours per gram)[1], but rechargeable batteries built with such anodes suffer from dendrite growth and low Coulombic efficiency (the ratio of charge output to charge input), preventing their commercial adoption[2,3]. The formation of inactive ('dead') lithium— which consists of both (electro)chemically formed Li^+ compounds in the solid electrolyte interphase and electrically isolated unreacted metallic Li^0 (refs [4,5])—causes capacity loss and safety hazards. Quantitatively distinguishing between Li^+ in components of the solid electrolyte interphase and unreacted metallic Li^0 has not been possible, owing to the lack of effective diagnostic tools. Optical microscopy[6], in situ environmental transmission electron microscopy[7,8], X-ray microtomography[9] and magnetic resonance imaging[10] provide a morphological perspective with little chemical information. Nuclear magnetic resonance[11], X-ray photoelectron spectroscopy[12] and cryogenic transmission electron microscopy[13,14] can distinguish between Li^+ in the solid electrolyte interphase and metallic Li^0, but their detection ranges are limited to surfaces or local regions. Here we establish the analytical method of titration gas chromatography to quantify the contribution of unreacted metallic Li^0 to the total amount of inactive lithium. We identify the unreacted metallic Li^0, not the (electro) chemically formed Li^+ in the solid electrolyte interphase, as the dominant source of inactive lithium and capacity loss. By coupling the unreacted metallic Li^0 content to observations of its local microstructure and nanostructure by cryogenic electron microscopy (both scanning and transmission), we also establish the formation mechanism of inactive lithium in different types of electrolytes and determine the underlying cause of low Coulombic efficiency in plating and stripping (the charge and discharge processes, respectively, in a full cell) of lithium metal anodes. We propose strategies for making lithium plating and stripping more efficient so that lithium metal anodes can be used for next-generation high-energy batteries.

Inactive lithium consists of diverse Li^+ compounds within the solid electrolyte interphase (SEI), such as LiF, Li_2CO_3, Li_2O, $ROCO_2Li$ (refs [15,16]), and of unreacted metallic Li^0 which is isolated by the SEI from the electronic conductive pathway. It is generally assumed that low Coulombic efficiency mostly arises from continuous repair of SEI fractures, which consumes both the electrolyte and active Li metal[17], although some researchers have suggested that unreacted metallic Li^0 may increase the tortuosity at the electrode/electrolyte interface and decrease the Coulombic efficiency in this way[18,19]. These assumptions and hypotheses are mostly based on observation, and the contribution to capacity loss from SEI formation has not been successfully quantified. Consequently, efforts to make Li metal a valid anode material may be misdirected. Differentiating and quantifying the Li^+ and Li^0 remaining on the electrode after stripping is key to understanding the mechanisms leading to capacity decay.

In our work, the pivotal difference exploited between the SEI Li^+ compounds and metallic Li^0 is their chemical reactivity: only the metallic Li^0 reacts with protic solvents (such as H_2O) and generates hydrogen gas (H_2). The solubility and reactivity of known SEI species with H_2O are listed in Extended Data Table 1. The possible presence of LiH (refs [20–22]) in inactive Li might affect the quantification of metallic Li^0 because LiH also reacts with water and produces H_2, so it was important to exclude this possibility in our results (see Methods for details). We combine H_2O titration (the step in which all metallic Li^0 is reacted) and gas chromatography (the subsequent step to quantify the H_2 generated in the reaction) into a single analytical tool, hereafter referred to as titration gas chromatography (TGC; schematic process in Extended Data Fig. 1), which is able to quantify the content of metallic Li^0 based on the reaction

$$2Li + 2H_2O \rightarrow 2LiOH + H_2\uparrow$$

When this is coupled with an advanced barrier ionization H_2 detector, the measurement of metallic Li^0 in the designed system is accurate to 10^{-7} g. The complete TGC methodologies are illustrated in Methods.

We then applied TGC to correlate the origin of inactive Li with the Coulombic efficiency in Li||Cu half-cells. As the Coulombic efficiency of Li metal varies greatly with electrolyte properties and current density, we compared two representative electrolytes, a high-concentration electrolyte (HCE; 4 M lithium bis(fluoro sulfonyl)imide (LiFSI) and 2 M lithium bis(trifluoromethane sulfonyl)imide (LiTFSI) in 1,2-dimethoxyethane (DME))[23] and a commercial carbonate electrolyte (CCE; 1 M $LiPF_6$ in ethylene carbonate/ethyl methyl carbonate (EC/EMC)), at three stripping rates (0.5 mA cm^{-2}, 2.5 mA cm^{-2} and 5.0 mA cm^{-2}; all plating at 0.5 mA cm^{-2} for 2 hours) . In addition, we examined six other electrolytes with a variety of salts, solvents and additives that frequently appear in the literature: 2 M LiFSI in dimethyl carbonate (DMC), 0.5 M LiTFSI in DME/1,3-dioxolane (DOL), 1 M LiTFSI–DME/DOL, 1 M LiTFSI–DME/DOL plus 2% $LiNO_3$, CCE plus Cs^+, and CCE plus fluoroethylene carbonate (FEC). Figure 1a shows that their first-cycle average Coulombic efficiencies have a broad range of values, from 17.2% to 97.1%. Representative voltage profiles are shown in Extended Data Fig. 2a, b. The total amount of inactive Li is equal to the capacity loss between the plating and stripping processes, displaying a linear relationship with Coulombic efficiency (Fig. 1d). The content of metallic Li^0 was directly measured by the TGC method. Once the amount of unreacted metallic Li^0 has been determined, the SEI Li^+ amount can be calculated, as the total amount of inactive Li (known) = unreacted metallic Li^0 (measured) + SEI Li^+.

The average capacity utilization under all conditions was quantified by the TGC, as summarized in Fig. 1b. The reversible capacity increases with increasing Coulombic efficiency. Interestingly, the unreacted metallic Li^0 amount increases significantly with the decrease of Coulombic efficiency, whereas the SEI Li^+ amount remains at a

[1]Materials Science and Engineering Program, University of California San Diego, La Jolla, CA, USA. [2]Department of NanoEngineering, University of California San Diego, La Jolla, CA, USA. [3]Department of Chemistry and Biochemistry, San Diego State University, San Diego, CA, USA. [4]Electrochemistry Branch, Sensors and Electron Devices Directorate, US Army Research Laboratory, Adelphi, MD, USA. [5]General Motors Research and Development Center, Warren, MI, USA. [6]These authors contributed equally: Chengcheng Fang, Jinxing Li. *e-mail: shirleymeng@ucsd.edu

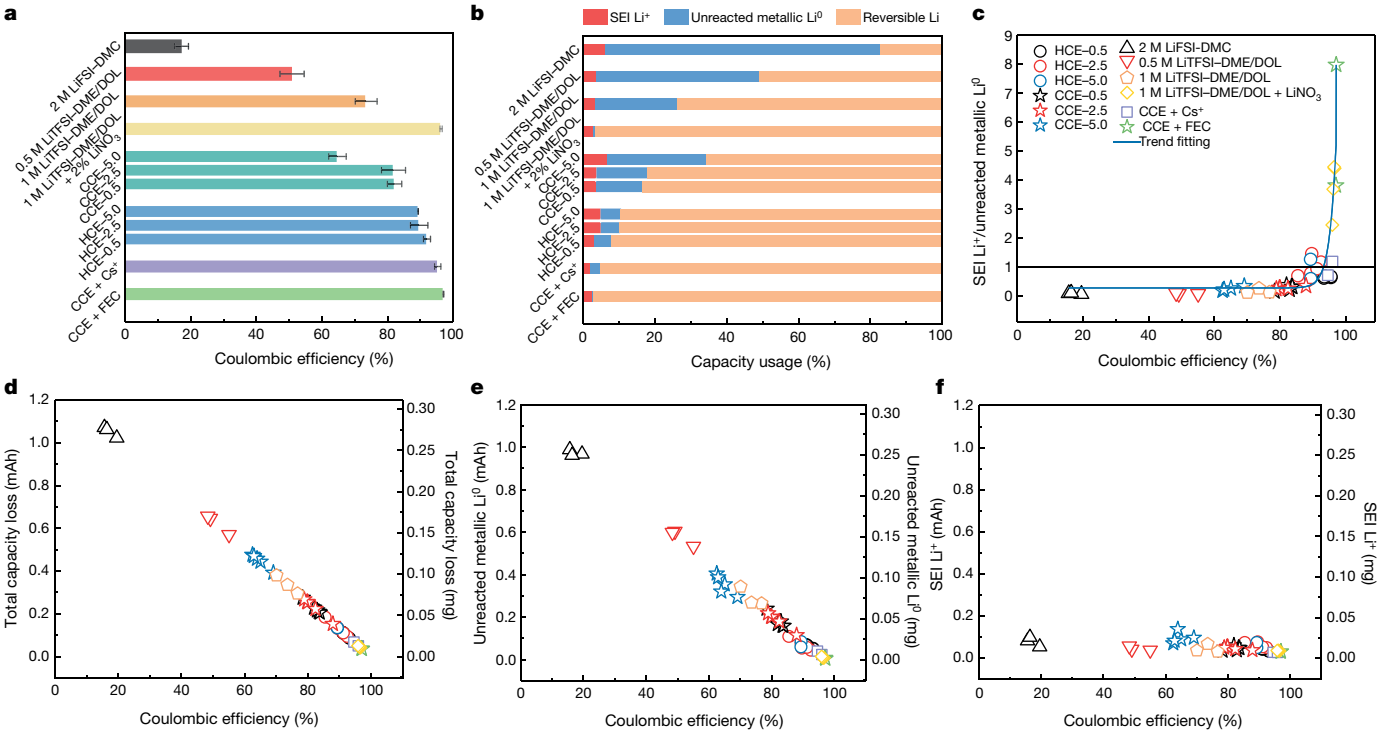

Fig. 1 | Quantitative differentiation of inactive Li by the TGC method. **a**, Average first-cycle Coulombic efficiency of Li||Cu cells under different testing conditions. Eight electrolytes (HCE, CCE, 2 M LiFSI–DMC, 0.5 M LiTFSI–DME/DOL, 1 M LiTFSI–DME/DOL, 1 M LiTFSI–DME/DOL + 2% $LiNO_3$, CCE + Cs^+ and CCE + FEC) and three stripping rates (0.5 mA cm^{-2}, 2.5 mA cm^{-2} and 5.0 mA cm^{-2} to 1 V) are used. In all electrolytes, Li was plated at 0.5 mA cm^{-2} for 2 hours (1 mAh cm^{-2}). HCE and CCE were selected for the three stripping rates study. Li formed in the rest electrolytes were stripped at 0.5 mA cm^{-2} to 1 V. At each condition, three to five cells were tested to obtain better statistics. The error bar represents the standard deviation of the average values of Coulombic efficiency. **b**, Analysis of capacity usage (SEI Li^+, unreacted metallic Li^0 and reversible Li) under different testing conditions by the TGC method. **c**, The ratio of SEI Li^+ to unreacted metallic Li^0 based on TGC quantification results. The blue line indicates exponential fitting. **d**, Total capacity loss as a function of Coulombic efficiency. (For unit conversion between milliampere-hours and milligrams of Li, see Extended Data Fig. 2f.) **e**, Amount of unreacted metallic Li^0 measured by the TGC method as a function of Coulombic efficiency. **f**, Calculated SEI Li^+ amount as a function of Coulombic efficiency.

constantly low level under all testing conditions. Further analysing the data, we found to our surprise that the amount of unreacted metallic Li^0 exhibits a linear relationship with loss of Coulombic efficiency (Fig. 1e), and this relationship is almost independent of the testing conditions. This implies that the Coulombic efficiency loss is governed by the formation of unreacted metallic Li^0. Meanwhile, the SEI Li^+ amount (Fig. 1f), as deduced from the total inactive Li and unreacted metallic Li^0, remains low and relatively constant under various testing conditions. The ratio of SEI Li^+ and unreacted metallic Li^0 (Li^+/Li^0) (Fig. 1c) reveals that the unreacted metallic Li^0 dominates the content of inactive Li ($Li^+/Li^0 < 1$) as well as the capacity loss when Coulombic efficiency is under about 95% in the first cycle. Once the Coulombic efficiency is higher than about 95%, the amount of SEI Li^+ starts to dominate. The ratios of unreacted metallic Li^0 to total inactive Li, and of SEI Li^+ to total inactive Li, are further shown in Extended Data Fig. 2c, d.

Increasing Li deposition capacity is reported to improve the first-cycle Coulombic efficiency[24]. To extend this method under different electrochemical conditions, we performed TGC tests on the CCE with Li plating capacities increased to 2 mAh cm^{-2}, 3 mAh cm^{-2} and 5 mAh cm^{-2}. The TGC results (Extended Data Fig. 3a, b) show that the SEI Li^+ amount increases with the extended deposition capacity; the improvement in Coulombic efficiency with increased Li deposition capacity is due to the reduction in the amount of unreacted metallic Li^0. At 3 mAh cm^{-2}, the Coulombic efficiency reaches 95.21%, while the ratio of SEI Li^+ to unreacted metallic Li^0 is measured to be 1.43, consistent with the above results.

Besides the first cycle, we also investigated the ratio of SEI Li^+ to unreacted metallic Li^0 after multiple cycles (two, five and ten) until the Coulombic efficiency is stabilized around 90% in CCE. As shown in Extended Data Fig. 3c, d, the Li^+/Li^0 ratio after one, two, five and ten cycles remains 0.27, 0.30, 0.27 and 0.34, respectively, indicating that the main capacity loss is from the unreacted metallic Li^0. The TGC results also reveal that the unreacted metallic Li^0 amount accumulates during extended cycles, indicating continuous consumption of active Li in Li metal batteries. These experiments, with varying electrolytes, additives, deposition capacities and cycles, all validate the TGC method as a reliable tool in studying the inactive Li.

Further examining the SEI components in HCE and CCE by X-ray photoelectron spectroscopy (XPS), we found that stripping rates have negligible impact on the relative contributions from SEI components (see Extended Data Fig. 4a, b). The TGC quantification analysis and XPS results establish that the contribution from the SEI Li^+ to the global content of inactive Li is not as large as commonly believed from previous studies[25–27].

To elucidate the formation mechanism of inactive Li, we use cryogenic focused ion beam–scanning electron microscopy (cryo-FIB–SEM) to explore the microstructures of inactive Li. HCE and CCE samples under different stripping rates are chosen for the morphological study. Cryogenic protection is critical here, because the highly reactive Li metal is not only sensitive to the electron beam but is also apt to react with the incident Ga ion beam to form a Li_xGa_y alloy at room temperature[28]. Completely different morphologies are generated by variations in stripping rates, even though all samples start from the same chunky Li deposits after plating at 0.5 mA cm^{-2} (Extended Data Fig. 5a–c). As the stripping rate increases, the morphology of inactive Li in HCE evolves from uniform sheets to local clusters (Fig. 2a–c) with a thickness increased from 500 nm to 2 μm (Fig. 2d–f). For the CCE, the individual whisker-like Li deposits (Extended Data Fig. 5d–f) become thinner after stripping (Fig. 2g–i), but the whole inactive Li layer becomes thicker in cross-section with the increased stripping rates

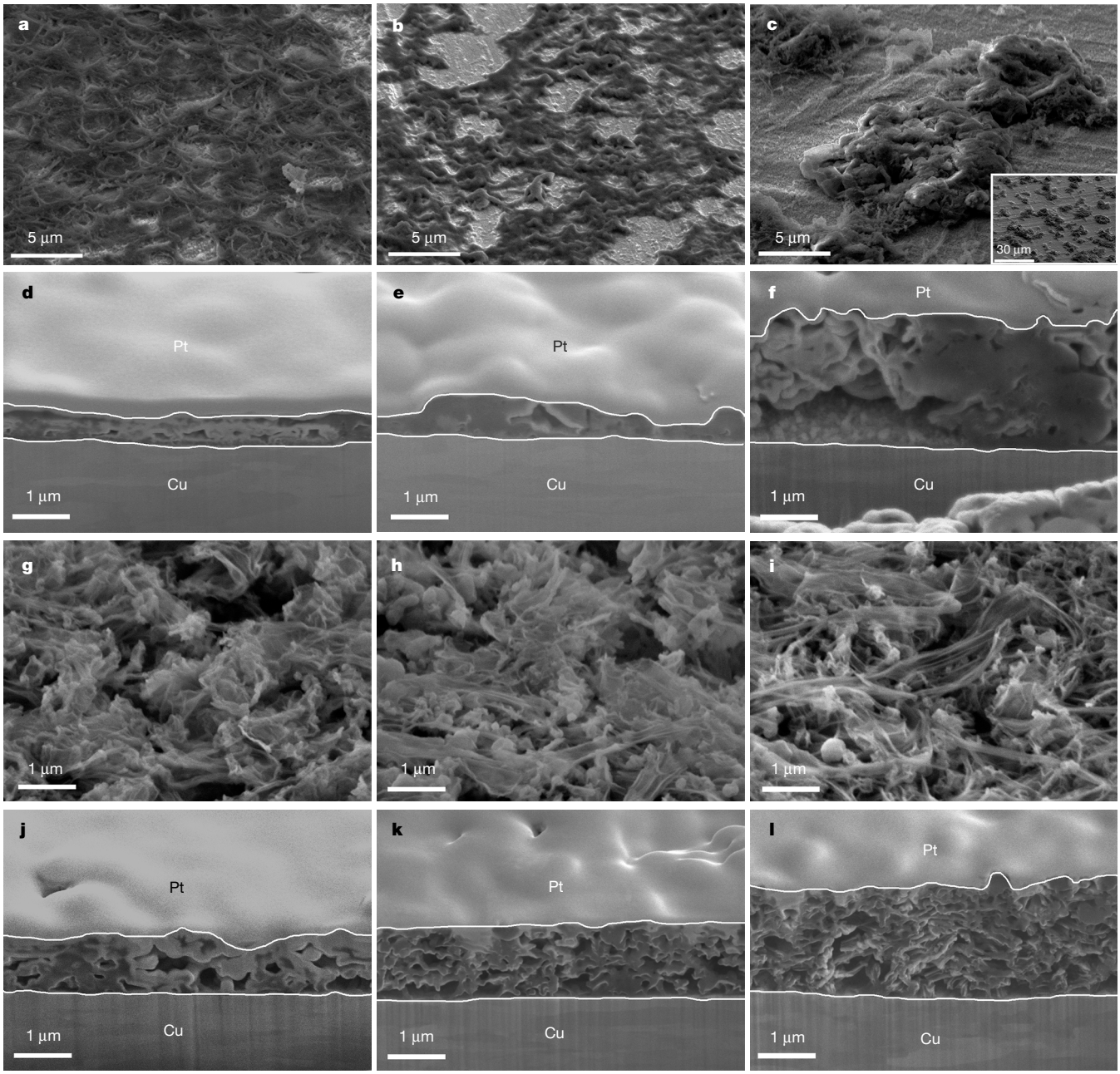

Fig. 2 | Microstructures of inactive Li generated in HCE and CCE imaged by cryo-FIB–SEM. a–f, Results for HCE. **g–l**, Results for CCE. **a–c**, **g–i**, Top view of the inactive Li at 52° tilted stage. **d–f**, **j–l**, Cross-sections obtained by cryo-FIB. Each column represents a different stripping rate: 0.5 mA cm^{-2} (**a**, **d**, **g**, **j**); 2.5 mA cm^{-2} (**b**, **e**, **h**, **k**); or 5.0 mA cm^{-2} (**c**, **f**, **i**, **l**).

(Fig. 2j–l), corresponding to the increased loss of Coulombic efficiency at high rates. It is worth noting that these residues exhibit poor connection to the current collector, indicating the loss of electronic conductive pathways.

We further used cryogenic transmission electron microscopy (cryo-TEM) to investigate the nanostructure of the inactive Li in HCE and CCE after stripping at 0.5 mA cm^{-2}. Sheet-like inactive Li appears in the HCE sample (Fig. 3a), whereas inactive Li in the CCE retains a whisker-like morphology (Fig. 3e). Based on the (110) lattice plane distance of body-centered cubic Li, the region that contains crystalline metallic Li^0 is highlighted in green in the high-resolution TEM (HRTEM) images for both electrolytes (Fig. 3b, f). Compared with the inactive Li obtained from CCE, a much smaller area of metallic Li^0 component is observed in HCE. This indicates that most of the deposited metallic Li^0 in HCE has been successfully stripped, corresponding to the high Coulombic efficiency. Whisker-like unreacted metallic Li^0 up to about 80 nm in length remains in the CCE sample and is well isolated by the surrounding SEI. The SEI components were determined by matching the lattice spacing in HRTEM images with their fast Fourier transform (FFT) patterns (Fig. 3c, g). The SEI components from more than 50 different sample positions have been analysed and are provided in Extended Data Fig. 5g, h for better statistics. Consistent with the XPS results (Extended Data Fig. 4), Li_2CO_3 and Li_2O constitute the majority of the SEI, which also contains LiF as well as other amorphous organic species for both electrolytes. The above observations from cryo-TEM are summarized in the schematic plot (Fig. 3d, h), which shows the form of inactive Li with two different morphologies at the nanoscale.

Correlating the inactive metallic Li^0 content with the micro- and nanostructures of inactive Li formed under different conditions, we propose mechanisms for the formation of inactive Li and for the stripping of Li metal. Two processes are involved in the stripping. The first

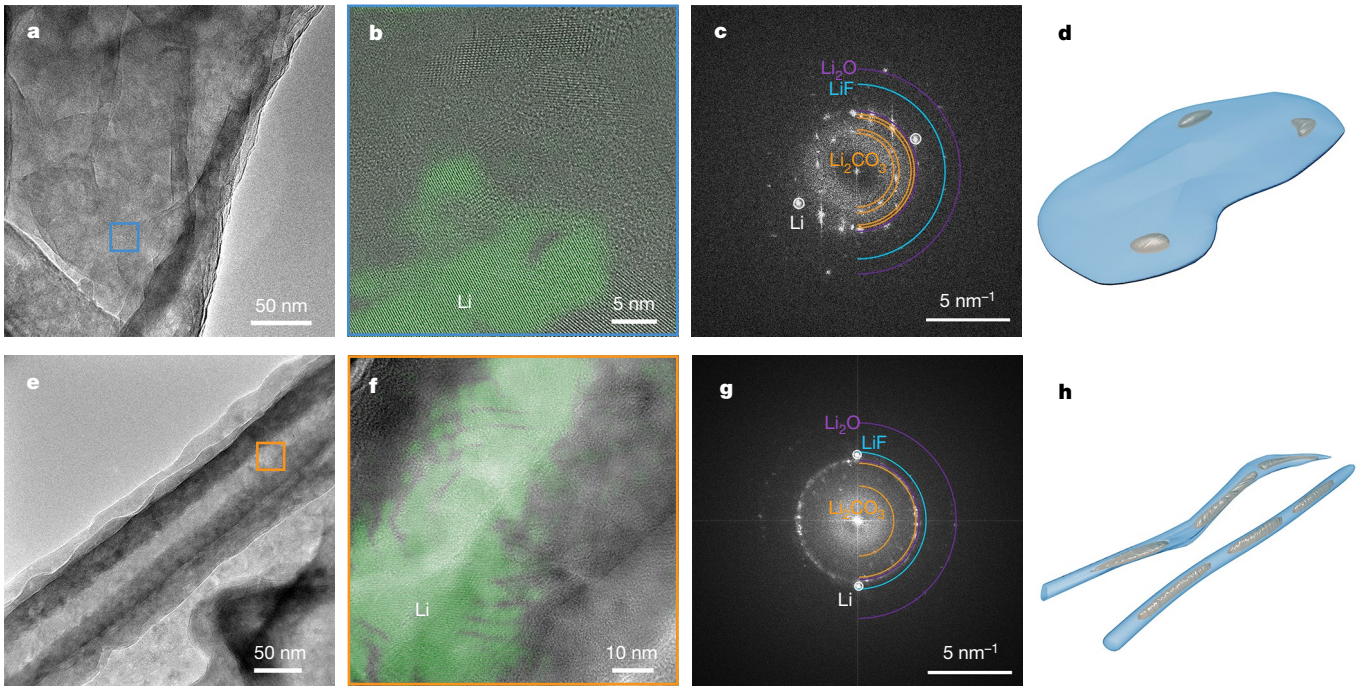

Fig. 3 | Nanostructures of inactive Li generated in HCE and CCE imaged by cryo-TEM. a–c, Results for HCE. **e–g**, Results for CCE. **a, e**, Inactive Li morphology at low magnifications for both electrolytes. **b, f**, HRTEM shows that a different amount of metallic Li^0 is wrapped by SEI in the two types of electrolyte. The highlighted metallic Li^0 region in green is identified through an inverse FFT process by applying mask filter on the origin FFT patterns. **c**, **g**, FFT patterns of corresponding HRTEM indicate the SEI component, which contains crystalline Li_2CO_3, Li_2O, and LiF. **d**, **h**, Schematic of inactive Li nanostructure in HCE (**d**) and CCE (**h**). A small area of metallic Li^0 is embedded in a sheet-like SEI layer for HCE, whereas a large bulk of metallic Li^0 is isolated in a whisker-like SEI layer in CCE.

of these is Li^+ dissolution: under the electric field, metallic Li^0 is oxidized to Li^+, which diffuses through the SEI layers and dissolves into the electrolyte. The second is SEI collapse: when the Li is removed, the SEI simultaneously shrinks and collapses towards the current collector. During these two dynamic processes, we emphasize an ignored but crucial aspect, the structural connection, which is defined as the capability of the active Li to maintain an electronic conductive network. The cryo-FIB–SEM and cryo-TEM images show that inactive Li^0 was either disconnected from the current collector or encapsulated by the insulating SEI, leading to the loss of structural connection. Obviously, for a Li deposit with whisker morphology and large tortuosity (Fig. 4a, taking the Li deposits formed in CCE as an example), the undesired microstructure can easily produce both ways of losing structural connection, leaving more unreacted metallic Li^0 during the stripping process. In

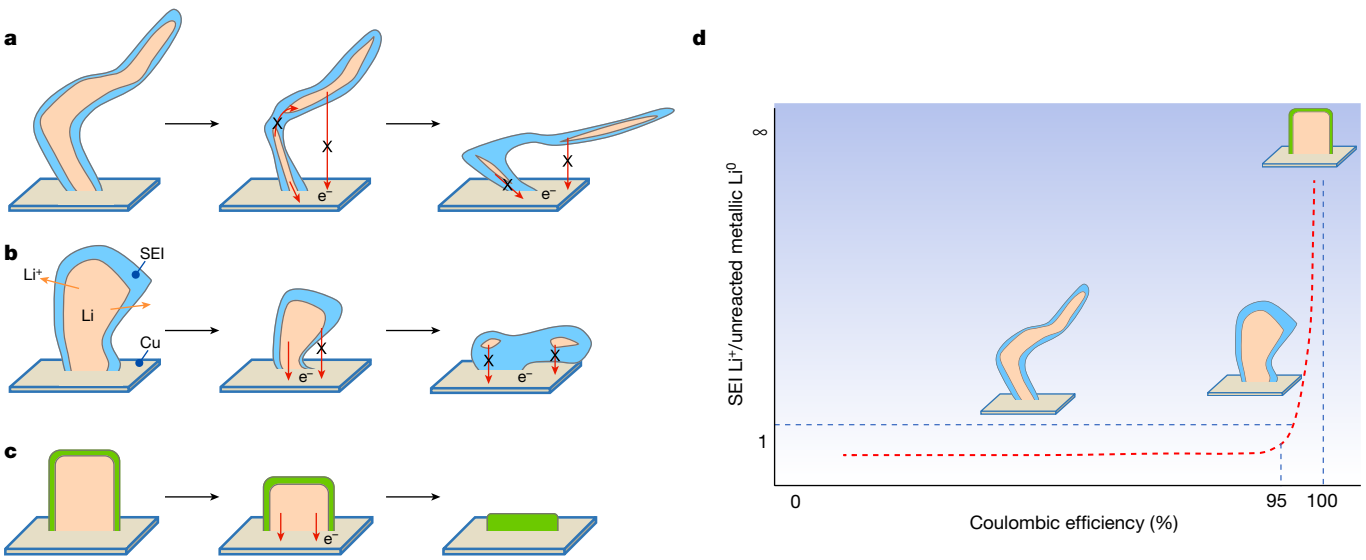

Fig. 4 | Schematic of inactive Li formation mechanism in different electrolytes, based on TGC quantification, cryo-FIB–SEM and cryo-TEM observation. a, Li deposits with whisker morphology and high tortuosity are more likely to lose electronic connection and maintain poor structural connection, leaving large amounts of unreacted metallic Li^0 trapped in SEI. **b**, Li deposits with large granular size and less tortuosity tend to maintain a good structural electronic connection, in which only small amounts of metallic Li^0 are stuck in tortuous SEI edges. **c**, An ideal Li deposit should have a columnar microstructure with a large granular size, minimum tortuosity and homogeneous distribution of SEI components, facilitating a complete dissolution of metallic Li^0. **d**, A general correlation of morphology of Li deposits, Coulombic efficiency and the ratio of SEI Li^+ to unreacted metallic Li^0.

contrast, dense Li with chunky morphology and low tortuosity (Fig. 4b, from HCE) has bulk integrity to maintain its structural connection and intimate contact with the current collector, resulting in a reduced presence of unreacted metallic Li^0 and high Coulombic efficiency. This is further evidenced by an advanced electrolyte with columnar microstructure and minimum tortuosity, which can deliver a first-cycle Coulombic efficiency as high as 96.2% (Extended Data Fig. 6a, b).

Based on the above observations and discussion, we propose the following strategies to improve Coulombic efficiency. An ideal architecture of deposited Li would promote structural connection and mitigate inactive Li formation, especially the formation of unreacted metallic Li^0. The ideal architecture includes the following. (1) The Li deposits should retain a columnar microstructure with a large granular size and minimum tortuosity, to minimize the unreacted metallic Li^0 residue (Fig. 4c, d). (2) The SEI should be both chemically and spatially homogeneous so that uniform Li^+ dissolution occurs. It should be mechanically elastic enough to accommodate the volume change. The SEI could be refilled during extended cycles, as schematized in Extended Data Fig. 6g. Using advanced electrolytes and artificial SEI may help to meet these requirements, while three-dimensional (3D) hosts that maintain electronic pathway and low tortuosity can contribute to constructing a durable structural connection and guiding the Li plating and stripping. To test this hypothesis, we compared 2D Cu foil and 3D Cu foam as the current collectors (Extended Data Fig. 6c, d). The initial Coulombic efficiency of 2D Cu foil and 3D Cu foam is 82% and 90%, respectively (Extended Data Fig. 6e). The increased Coulombic efficiency in the latter is attributed to the reduced amount of unreacted metallic Li^0 (Extended Data Fig. 6f), despite the fact that the amount of SEI Li^+ increases from 21.5% to 62.7% owing to the higher surface area of 3D Cu foam. Therefore, although the 3D current collector helps in maintaining a good electronic conductive network, it is necessary to control its surface properties to minimize SEI formation. The structural connection can be further enforced by applying external pressure. Slight stacking pressure can improve cycling performance[29,30]. In our proposed model, we believe that pressure promotes structural collapse towards the current collector, thus leading to better structural connection which mitigates the generation of unreacted metallic Li^0. We found the critical pressure in maintaining good structural connection to be as low as about 5 psi, which should not damage any SEI (Extended Data Fig. 6h). A fast stripping rate could accelerate the Li^+ dissolution but may destroy the structural connection, because Li at the tip of column or whiskers could fail to keep pace with the rapid dynamic. Overall, the tools established here can be universally extended to examine various battery chemistries under different conditions, with the aim of developing a better battery that is energy-dense and safe.

Online content

Any methods, additional references, Nature Research reporting summaries, source data, extended data, supplementary information, acknowledgements, peer review information; details of author contributions and competing interests; and statements of data and code availability are available at https://doi.org/10.1038/s41586-019-1481-z.

Received: 21 January 2019; Accepted: 12 June 2019;
Published online 21 August 2019.

1. Tarascon, J. M. & Armand, M. Issues and challenges facing rechargeable lithium batteries. *Nature* **414**, 359–367 (2001).
2. Lin, D., Liu, Y. & Cui, Y. Reviving the lithium metal anode for high-energy batteries. *Nat. Nanotechnol.* **12**, 194–206 (2017).
3. Xu, W. et al. Lithium metal anodes for rechargeable batteries. *Energy Environ. Sci.* **7**, 513–537 (2014).
4. Yoshimatsu, I., Hirai, T. & Yamaki, J. Lithium electrode morphology during cycling in lithium cells. *J. Electrochem. Soc.* **135**, 2422–2427 (1979).
5. Lu, D. et al. Failure mechanism for fast-charged lithium metal batteries with liquid electrolytes. *Adv. Energy Mater.* **5**, 1400993 (2015).
6. Wood, K. N., Noked, M. & Dasgupta, N. P. Lithium metal anodes: toward an improved understanding of coupled morphological, electrochemical, and mechanical behavior. *ACS Energy Lett.* **2**, 664–672 (2017).
7. Bai, P., Li, J., Brushett, F. R. & Bazant, M. Z. Transition of lithium growth mechanisms in liquid electrolytes. *Energy Environ. Sci.* **9**, 3221–3229 (2016).
8. Mehdi, B. L. et al. Observation and quantification of nanoscale processes in lithium batteries by operando electrochemical (S)TEM. *Nano Lett.* **15**, 2168–2173 (2015).
9. Harry, K. J., Hallinan, D. T., Parkinson, D. Y., Macdowell, A. A. & Balsara, N. P. Detection of subsurface structures underneath dendrites formed on cycled lithium metal electrodes. *Nat. Mater.* **13**, 69–73 (2013).
10. Chandrashekar, S. et al. ^{7}Li MRI of Li batteries reveals location of microstructural lithium. *Nat. Mater.* **11**, 311–315 (2012).
11. Bhattacharyya, R. et al. In situ NMR observation of the formation of metallic lithium microstructures in lithium batteries. *Nat. Mater.* **9**, 504–510 (2010).
12. Xu, C. et al. Interface layer formation in solid polymer electrolyte lithium batteries: an XPS study. *J. Mater. Chem. A* **2**, 7256–7264 (2014).
13. Li, Y. et al. Atomic structure of sensitive battery materials and interfaces revealed by cryo-electron microscopy. *Science* **358**, 506–510 (2017).
14. Wang, X. et al. New insights on the structure of electrochemically deposited lithium metal and its solid electrolyte interphases via cryogenic TEM. *Nano Lett.* **17**, 7606–7612 (2017).
15. Cheng, X. B. et al. A review of solid electrolyte interphases on lithium metal anode. *Adv. Sci.* **3**, 1–20 (2015).
16. Zheng, J., Lochala, J. A., Kwok, A., Deng, Z. D. & Xiao, J. Research progress towards understanding the unique interfaces between concentrated electrolytes and electrodes for energy storage applications. *Adv. Sci.* **4**, 1700032 (2017).
17. Li, S. et al. Developing high-performance lithium metal anode in liquid electrolytes: challenges and progress. *Adv. Mater.* **30**, 1706375 (2018).
18. Steiger, J., Kramer, D. & Mönig, R. Microscopic observations of the formation, growth and shrinkage of lithium moss during electrodeposition and dissolution. *Electrochim. Acta* **136**, 529–536 (2014).
19. Chen, K.-H. et al. Dead lithium: mass transport effects on voltage, capacity, and failure of lithium metal anodes. *J. Mater. Chem. A* **5**, 11671–11681 (2017).
20. Zachman, M. J., Tu, Z., Choudhury, S., Archer, L. A. & Kourkoutis, L. F. Cryo-STEM mapping of solid–liquid interfaces and dendrites in lithium-metal batteries. *Nature* **560**, 345–349 (2018).
21. Aurbach, D. & Weissman, I. On the possibility of LiH formation on Li surfaces in wet electrolyte solutions. *Electrochem. Commun.* **1**, 324–331 (1999).
22. Hu, Y. Y. et al. Origin of additional capacities in metal oxide lithium-ion battery electrodes. *Nat. Mater.* **12**, 1130–1136 (2013).
23. Alvarado, J. et al. Bisalt ether electrolytes: a pathway towards lithium metal batteries with Ni-rich cathodes. *Energy Environ. Sci.* **12**, 780–794 (2019).
24. Adams, B. D., Zheng, J., Ren, X., Xu, W. & Zhang, J. G. Accurate determination of Coulombic efficiency for lithium metal anodes and lithium metal batteries. *Adv. Energy Mater.* **8**, 1702097 (2017).
25. Lu, J., Wu, T. & Amine, K. State-of-the-art characterization techniques for advanced lithium-ion batteries. *Nat. Energy* **2**, 17011 (2017).
26. Lee, H. et al. Suppressing lithium dendrite growth by metallic coating on a separator. *Adv. Funct. Mater.* **27**, 1704391 (2017).
27. Zheng, J. et al. Highly stable operation of lithium metal batteries enabled by the formation of a transient high-concentration electrolyte layer. *Adv. Energy Mater.* **6**, 1–10 (2016).
28. Saint, J., Morcrette, M., Larcher, D. & Tarascon, J. M. Exploring the Li-Ga room temperature phase diagram and the electrochemical performances of the LixGay alloys vs. Li. *Solid State Ion.* **176**, 189–197 (2005).
29. Yin, X. et al. Insights into morphological evolution and cycling behaviour of lithium metal anode under mechanical pressure. *Nano Energy* **50**, 659–664 (2018).
30. Lee, H. et al. Electrode edge effects and the failure mechanism of lithium-metal batteries. *ChemSusChem* **11**, 3821–3828 (2018).

METHODS

Electrochemical testing. Coulombic efficiency was measured in Li||Cu coin cells: Li metal (1 mm thick, 0.5 inch in diameter), two pieces of separators (Celgard) and Cu foil (0.5 inch in diameter) were sandwiched in CR2032 coin cells with a spacer and a spring, and crimped inside an Ar-filled glovebox. A 50 μl amount of the electrolyte was added in each cell. HCE consists of 4 M LiFSI (battery grade; Oakwook Products, Inc.) + 2 M LiTFSI (battery grade; Solvay) in DME (anhydrous, >99.5%; BASF). CCE consists of 1 M $LiPF_6$ (battery grade, BASF) in EC/EMC (battery grade, BASF) (3:7 by weight) with 2 wt% of vinylene carbonate (battery grade, BASF). CCE + Cs^+ contains 50 mM of $CsPF_6$ (Synquest Laboratory). CCE + FEC contains 10 wt% of FEC (anhydrous, >99%, Sigma-Aldrich). DOL (anhydrous, >99.5%) and $LiNO_3$ were purchased from Sigma-Aldrich. Cells for TGC are plating at 0.5 mA cm^{-2} for 1 mAh cm^{-2} and stripping at various rates (0.5 mA cm^{-2}, 2.5 mA cm^{-2} and 5 mA cm^{-2}) to 1 V, unless otherwise specified.

Titration gas chromatography. Extended Data Fig. 1 demonstrates the typical processes of the TGC method for the inactive Li quantification, including the following six main steps. (1) After plating and stripping, the Li||Cu coin cell was disassembled in an Ar-filled glovebox. (2) While still in the glovebox, both the Cu foil and separator on the Cu foil side were harvested without washing and sealed in a container with an inside pressure of 1 atm by a rubber septum which is stable against water. (3) After transferring the sample container out of the glovebox, we injected 0.5 ml of H_2O into the container to react with the inactive Li completely. (4) A gas-tight syringe was used to transfer 30 μl of the resultant gas from the container into the gas chromatography (GC) system. (5) The amount of H_2 was measured by the GC. (6) The content of the metallic Li^0 was determined by converting the corresponding H_2 amount according to a pre-established standard calibration curve (Extended Data Fig. 7b). All the processes minimize the potential damage and contamination during sample transfer, to obtain reliable results.

In the GC column, the stationary phase has a different affinity with different species, so that gas species can be differentiated by retention time. Extended Data Fig. 8a shows the GC chromatograms of background gases from a well-sealed empty container in the Ar-filled glovebox. The peaks at 1.45 min, 2.42 min and 3.21 min represent Ar, N_2 and CH_4, respectively. When an H_2O titration process is applied to a small piece of pure Li metal, H_2 will be generated. The H_2 characteristic peak appears at 1.05 min, as shown in Extended Data Fig. 8b.

Source of N_2 in the gas chromatograms. Note that N_2 detected from the GC comes from the gas sampling process, instead of existing in the reaction container. As schematized in the TGC process in Extended Data Fig. 1, the inactive Li samples were loaded and sealed into the reaction container in an Ar-filled and N_2-free glovebox. After the samples were taken out of the glovebox, 0.5 ml of pure H_2O was injected into the container and reacted with the inactive Li sample. This is an air-free process. A gas-tight syringe was then used to take the gas sample for GC injection and measurement. There is a small amount of air left in the needle space of the gas-tight syringe. Moreover, in the GC injection process, when the needle breaks the septum, a tiny amount of air might be introduced into the GC column. Even though the air peak is inevitable for the injection gas sampling method, the inactive Li samples have indeed all been reacted in advance and were never exposed to N_2.

We carried out the following tests to demonstrate that the N_2 comes from the air during sampling and that the presence of air has negligible impact on the inactive Li (H_2) quantification. First, we measured the gas in the blank container without any inactive Li, which has been well sealed in the Ar-filled glovebox. If the N_2 comes from the reaction container, the intensity of the N_2 peaks will vary proportionally to the injected gas amount into the GC. We took different amounts of gas sample from the blank container and performed GC measurement. As shown in Extended Data Fig. 8c, the N_2 peak intensities remain almost identical for injection amounts varying from 5 to 30 μl. The same result was obtained when H_2O titration was performed on inactive Li. The measured H_2 content increase as a function of injected gas amount while the N_2 content remains almost constant (Extended Data Fig. 8d). Noting that the reaction container is sealed in the Ar-filled glovebox, the Ar peak is saturated even if only 5 μl of sample gas is injected and remains unchanged in all measurements. The invariability of N_2 peaks is not because of saturation in the previous measurements, since the intensity of the N_2 peak increases significantly after purposely injecting 10 μl of air (Extended Data Fig. 8e). Therefore, we have confirmed that the N_2 comes from the injection sampling process and it will not have any chemical reaction with the inactive Li samples. Moreover, the H_2 quantification is not influenced by the injection sampling process.

Possible existence of LiH. Besides the SEI species listed in Extended Data Table 1, there have been mixed reports regarding the existence of LiH in Li metal electrodes[20–22]. There are two possible scenarios in which LiH may exist in the Li metal electrodes: (1) LiH may exist within the SEI as an electrochemical reduction product at excessively negative potentials[21,22]; (2) LiH may largely exist in the bulk electrode as mossy dendrites[20]. To examine the possible influence from LiH in SEI, we repeatedly polarized the current collectors above 0 V, so that only SEI forms without metallic Li^0 deposition[31]. For the electrolytes investigated in this work, after such cyclic polarizations between 0 V and 1 V for ten cycles, the TGC detected no H_2 from all SEI–water reactions (Extended Data Fig. 9a-h), indicating that LiH does not exist in the SEIs. To examine the possible influence from LiH in bulk inactive Li, we changed the titration solution from H_2O to D_2O, which can distinguish LiH and metallic Li^0 by producing HD and D_2, respectively, based on the following reactions: (1) $LiH + D_2O = LiOD + HD\uparrow$; (2) $2Li + 2D_2O = 2LiOD + D_2\uparrow$. Differentiating HD and D_2 was then achieved based on partial pressure analysis by residual gas analyser (RGA)[32]. From the RGA results (Extended Data Fig. 9i–n), we confirmed that LiH does not exist in the bulk inactive Li generated by the electrolyte systems of low Coulombic efficiency. The exclusion of LiH from either SEI or bulk inactive Li confirms that the conclusions drawn from the TGC analysis should be reliable and free of interference from possible LiH species.

Calibration. The H_2 concentration was calibrated and measured using a Shimadzu GC-2010 Plus Tracera equipped with a barrier ionization discharge (BID) detector. Helium (99.9999%) was used as the carrier gas. Split temperature was kept at 200 °C with a split ratio of 2.5 (split vent flow: 20.58 ml min^{-1}, column gas flow: 8.22 ml min^{-1}, purge flow: 0.5 ml min^{-1}). Column temperature (RT-Msieve 5A, 0.53 mm) was kept at 40 °C. A BID detector was kept at 235 °C, and BID detector gas flow rate was 50 ml min^{-1}. All calibration and sample gases were immediately collected via a 50 μl Gastight Hamilton syringe before injection. For calibration of H_2 concentration, 1,500 p.p.m. of H_2 gas was produced by reacting high-purity sodium with DI water in a septum sealed glass vial. We collected 5 μl, 10 μl, 15 μl, 20 μl, 25 μl and 30 μl of the H_2 gas produced, corresponding to 250 p.p.m., 500 p.p.m., 750 p.p.m., 1,000 p.p.m., 1,250 p.p.m. and 1,500 p.p.m., respectively, and injected them into the GC. The calibration curve was plotted and fitted with H_2 concentration versus H_2 peak area as measured by the GC. The as-established H_2 calibration curve ($H_{2,ppm}$ versus detected H_2 area) and equation are shown in Extended Data Fig. 7a. To acquire the exact number of H_2 molecules within the container, the H_2 concentration calibration curve was converted to a calibration curve in terms of the mole number of H_2 as a function of detected area based on the following two conditions: (1) 1 p.p.m. = 4.08×10^{-8} mmol ml^{-1} (1 atm, 298 K); (2) container volume (30 ± 0.5 ml).

The mole number of H_2 calibration curve established a direct relationship between H_2 area reported by the GC software and the number of H_2 molecules in the fixed TGC set-up, making the following inactive Li measurement independent of slight pressure change. Based on the chemical reaction $2Li + 2H_2O \rightarrow 2LiOH + H_2\uparrow$, the standard calibration curve and the equation for Li metal mass (m_{Li}) as a function of the detected H_2 area are obtained and shown in Extended Data Fig. 7b.

Validation of the GC measurement. (1) The H_2 concentration in p.p.m. as a function of GC detected H_2 area (Extended Data Fig. 7a) was verified by using the certified GASCO H_2 calibration test gas. (2) We then used commercial Li metal of known mass to verify the relationship established for m_{Li} versus detected H_2 area (Extended Data Fig. 7b). We carefully weighed nine pieces of commercial Li metal with mass ranging from 0.54 mg to 1.53 mg in the Ar-filled glovebox with a five-digit balance (10^{-5} g) and then performed the TGC measurement. The detected H_2 area as a function of the Li metal mass from the nine pieces of Li metal is shown in Extended Data Fig. 7c. The result shows that the mass of Li metal is linearly related ($R^2 = 99.8\%$) to the detected H_2 area, indicating the validity of the TGC system for quantifying metallic Li^0. In reverse, we calculated the Li metal mass from the detected H_2 area using the relationship of m_{Li} versus detected H_2 area. The TGC-measured and balance-measured Li metal masses are compared in Extended Data Fig. 7d. The exact values of TGC-measured and balance-measured Li metal masses are listed in Extended Data Fig. 7e. The negligible differences between the TGC quantification and balance measurement indicate the validity and accuracy of the TGC method. The significant digit of the balance is 0.01 mg (10^{-5} g), as marked in red in Extended Data Fig. 7e, whereas that of the TGC is 0.0001 mg (0.1 μg, 10^{-7} g), which has been demonstrated in the limit of detection/limit of quantification (LOD/LOQ) analysis. Thus, the minimal difference between the two quantification methods is mainly ascribed to the inaccuracy of the balance, which has a precision two orders of magnitude smaller than the TGC.

LOD/LOQ analysis. The concentration of hydrogen in the air is 0.000053%. To get the LOD/LOQ values, 30 μl of the air sample was injected into GC by the same gas-tight syringe as used for the hydrogen measurement and repeated for a total of 10 times. The results are listed in Extended Data Fig. 7f. Based on the definition of LOD/LOQ, the calculated LOD/LOQ from the table is 16.44 p.p.m. and 49.81 p.p.m., respectively, corresponding to 0.28 μg and 0.84 μg of metallic Li^0 in the designed TGC system.

Inactive Li sample measurement. After stripping under various conditions, Li||Cu cells were disassembled inside an Ar-filled glovebox ($H_2O < 0.5$ p.p.m.). The Cu foil and separator near the Cu foil side with inactive Li residue on top were placed into a 30 ml container without washing. The container was sealed by a rubber septum and further capped by a stainless-steel/copper ring for safety and to minimize the deformation of the rubber septum when gas was generated later. The

internal pressure of the sealed container was adjusted to 1 atm by connecting the container and glovebox environment (0 mbar) with an open-ended syringe needle. After transferring the sealed container out of the glovebox, 0.5 ml of water was injected into the container, allowing complete reaction of inactive Li residue with water. An excess amount of H_2O was added to react with all the inactive metallic Li^0, leading to complete conversion to the H_2 products. The Cu foil became shiny and the separator normally became clean when reactions finished, indicating a complete reaction of the inactive Li with H_2O. The as-generated gases were then well dispersed and mixed by shaking the container to prevent H_2 accumulation on top of the container. Then a gas-tight syringe was used to quickly take 30 μl of the well-mixed gas and to inject it into the GC for H_2 measurement. The GC-measured H_2 areas as a function of cell Coulombic efficiency are shown in Extended Data Fig. 2e. The conversion between mAh and mg of Li is shown in Extended Data Fig. 2f.

Safety considerations. Li is electrochemically inactive, but chemically hyperactive due to the high surface areas which may lead to serious potential safety hazards[33]. Inactive Li quantification using the TGC method should be done carefully, taking the following aspects into consideration:

(1) The proper amount of inactive Li for TGC measurement. The minimum amount of inactive metallic Li that has been measured is as low as 1 μg (~0.004 mAh). The maximum amount measured in the present work is ~1.6 mg, corresponding to ~6 mAh. It is generally preferred to reduce the amount of inactive Li sample, as the GC with an advanced H_2 detector can be very sensitive (1 p.p.m.). The greater the amount of H_2 generated, the more dangerous it could be.

(2) The reaction container must be completely sealed inside the Ar-filled glovebox before it is taken out, to avoid O_2 and moisture entering the container. Moisture in air influences the measurement accuracy, and O_2 may lead to an explosion when a large amount of water reacts with inactive Li.

(3) Stainless steel/copper rings should be used to minimize the deformation of the rubber septum when H_2 is generated inside the reaction container after water titration, and to prevent potential explosion due to the increased internal pressure.

(4) Waste gas in the container after TGC measurement should be disposed of in a fume hood to avoid regional H_2 accumulation which can lead to an explosion (explosive limits of H_2 in air range from about 18% to 60%; the flammable limits are 4–75%).

Cryogenic focused ion beam scanning electron microscopy. The inactive Li samples on Cu foil were disassembled and washed with anhydrous DME (for HCE) or DMC (for CCE) in the Ar-filled glovebox. The samples were mounted on the SEM sample holder in the glovebox, then transferred to a FEI Helios NanoLab Dualbeam. Platinum was deposited for surface protection from the ion beam: 100 nm of Pt was deposited using the electron beam at 5 kV, 0.8 nA; 300 nm of Pt was deposited using the ion beam at 30 kV, 0.1 nA. The stage was cooled with liquid nitrogen to −180 °C or below. Sample cross-sections were exposed using a 1 nA ion beam current and 100 ns dwell time, and cleaned twice at 0.5 nA and 0.1 nA, respectively. SEM images were taken with an Everhart-Thornley Detector (ETD) at 5 kV.

Cryogenic transmission electron microscopy. The cryo-TEM sample for HCE was directly deposited and stripped on a lacey carbon grid in the Li||Cu half-cell. The sample for CCE was prepared by peeling the inactive Li from Cu foil cycled in the half-cell, and then depositing it onto the same type of TEM grid. Both half-cells were plated at 0.5 mA cm^{-2} for 2 hours and then stripped to 1 V at the same rate. Both TEM samples were slightly rinsed with DME/DMC in the Ar-filled glovebox to remove trace Li salt. Once dry, the samples were sealed in airtight bags and plunged directly into a bath of liquid nitrogen. The airtight bags were then cut and the TEM grids were immediately immersed in liquid nitrogen. Then the grids were mounted onto a TEM cryo-holder (Gatan) via a cryo-transfer station. In short, the whole TEM sample preparation and transfer process prevents any contact of Li metal with the air at room temperature. TEM characterizations were carried out on JEOL JEM-ARM300CF at 300 kV and JEM-2100F at 200 kV. HRTEM images were taken at a magnification of ×500,000 with a Gatan OneView Camera (full 4,000 × 4,000 pixel resolution) when the temperature of samples reached about 100 K. The FFT pattern and inverse FFT image after mask filtering were analysed with DigitalMicrograph software.

X-ray photoelectron spectroscopy. After a plating/stripping process, cells were disassembled in an Ar-filled glovebox with $H_2O < 0.5$ p.p.m. Cu foils with inactive Li residue were gently and thoroughly rinsed by DME (for HCE) and DMC (for CCE) to remove residual surface Li salts. The rinsed electrodes were sealed in an airtight stainless-steel container and transferred into the glovebox connected to the XPS chamber. XPS was performed with a Kratos AXIS Supra, with the Al anode source operated at 15 kV. The chamber pressure was $<10^{-8}$ torr during all measurements. All XPS measurements were collected with a spot size 300 μm by 700 μm with a charger neutralizer during acquisition. Survey scans were collected with a 1.0 eV step size, followed by high-resolution scans collected with a step size of 0.05 eV. Fittings of the XPS spectra were performed with CasaXPS software (version 2.3.15, Casa Software Ltd) to estimate the atomic compositions and chemical species. All species (Li 1*s*, F 1*s*, O 1*s* and C 1*s*) were fitted using a Shirley type background. High-resolution spectra were calibrated using the C 1*s* peak at 284.6 eV. The peak positions and areas were optimized by a Levenberg–Marquardt least-squares algorithm using 70% Gaussian and 30% Lorentzian line shapes. Quantification was based on relative sensitivity factors. The curve fit for the core peaks was obtained using a minimum number of components to fit the experimental curves.

Residual gas analyser. To exclude the potential influence on TGC (H_2) quantification from LiH, which may exist in the bulk electrode as mossy dendrite, we designed an alternative approach to distinguish between LiH and metallic Li^0 by changing the titration solution from H_2O to D_2O, which reacts with LiH and Li to produce HD and D_2, respectively, followed by differentiating between HD and D_2 based on partial pressure analysis by RGA. The base pressure in the vacuum chamber is ~8×10^{-8} torr. The gas mixtures were introduced into the chamber using an MKS pressure/flow control valve controlled by a computer. The partial pressures of gases in the system were measured using an SRS RGA with a detection limit down to 10^{-11} torr. The turbo pump and backing pump used in this vacuum system were specially designed for handling highly corrosive gases. This setup provides a wide-range partial pressure control (10^{-11} torr to 10^{-4} torr) and allow the identification of the different gas molecules including hydrogen isotopes present in the system under high vacuum conditions. Before measuring each sample, the whole system was pumped down to high vacuum (10^{-8} torr) to minimize the possibility of contamination.

Data availability

The data that support the findings of this study are available from the corresponding author on reasonable request.

31. Wood, S. M. et al. Predicting calendar aging in lithium metal secondary batteries: the impacts of solid electrolyte interphase composition and stability. *Adv. Energy Mater.* **8**, 1–6 (2018).
32. Drenik, A. et al. Evaluation of the plasma hydrogen isotope content by residual gas analysis at JET and AUG. *Phys. Scr.* **T170**, 014021 (2017).
33. Xu, K. Nonaqueous liquid electrolytes for lithium-based rechargeable batteries. *Chem. Rev.* **104**, 4303–4418 (2004).

Acknowledgements This work was supported by the Office of Vehicle Technologies of the US Department of Energy through the Advanced Battery Materials Research (BMR) Program (Battery500 Consortium) under contract DE-EE0007764. Cryo-FIB was performed at the San Diego Nanotechnology Infrastructure, a member of the National Nanotechnology Coordinated Infrastructure, which is supported by the US National Science Foundation (NSF) (grant ECCS-1542148). We acknowledge the UC Irvine Materials Research Institute for the use of the cryo-electron microscopy and XPS facilities, funded in part by the NSF Major Research Instrumentation Program under grant CHE-1338173. The partial pressure measurements and analysis were done using a unique RGA based high vacuum gas evolution system developed under the guidance of I. K. Schuller's laboratory at UC San Diego. The development of this system were supported by the US Department of Energy, Office of Science, Basic Energy Science (BES) under grant DE FG02 87ER-45332. C.F. thanks D. M. Davies for his suggestions on the manuscript and Shuang Bai for her assistance with the TEM experiment. J.L. thanks W. Wu for helping on figure design.

Author contributions C.F., J.L., X.W. and Y.S.M. conceived the ideas. C.F. designed and implemented the TGC system. C.F. designed and performed the TGC, cryo-FIB–SEM, XPS experiments and data analysis. M.Z. collected the cryo-TEM data. C.F., M.Z. and B.L. interpreted TEM data. Y.Z., C.F. and M.C. prepared samples for characterizations. J.Z.L. and Y.Y. helped to set up cryo-FIB instrumentation. F.Y., N.W. and J.G. helped with GC set up and calibration. C.F. and M.-H.L. performed the RGA experiment. J.A., M.A.S. and K.X. formulated and provided the HCE electrolyte. L.Y. and M.C. formulated and provided the GM electrolyte. J.L. and C.F. wrote the manuscript. All authors discussed the results and commented on the manuscript. All authors have approved the final manuscript.

Competing interests The authors declare no competing interests.

Additional information

Correspondence and requests for materials should be addressed to Y.S.M.

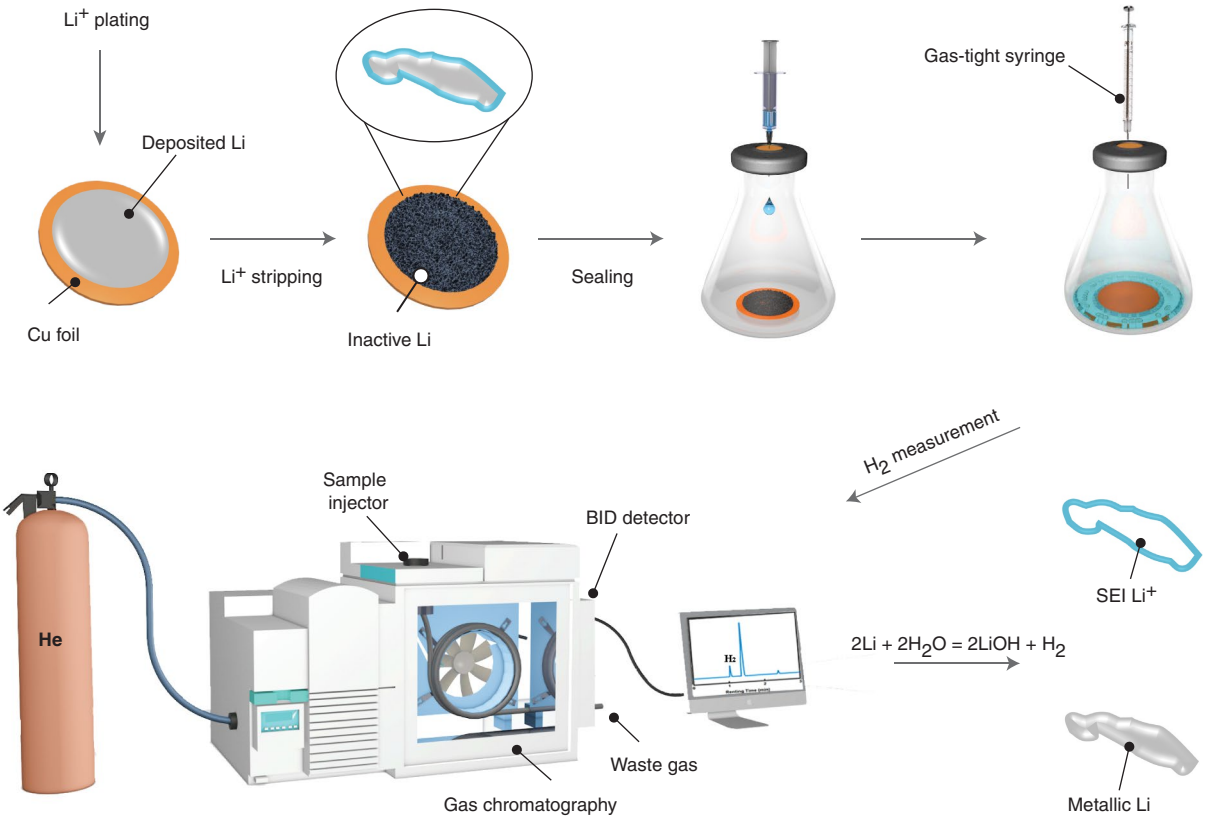

Extended Data Fig. 1 | Schematic working principle of the TGC method. By combining [H_2O titration on an inactive Li sample and H_2 quantification by GC, the amount of metallic Li^0 is calculated based on the chemical reaction $2Li + 2H_2O \rightarrow 2LiOH + H_2\uparrow$.

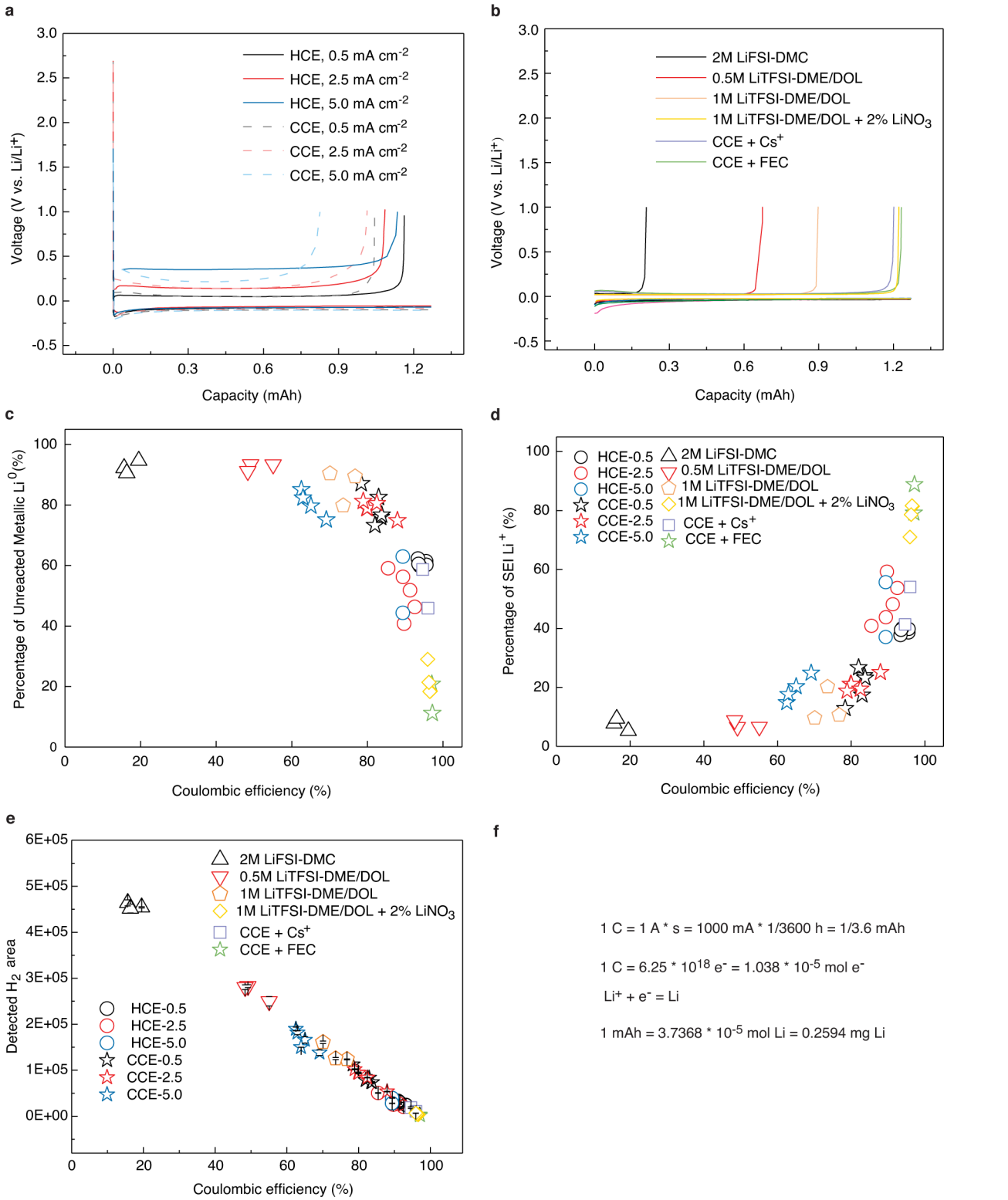

Extended Data Fig. 2 | Supplementary materials for TGC analysis. **a**, **b**, Representative voltage profiles of Li||Cu cells in (**a**) HCE and CCE, plating at 0.5 mA cm^{-2} for 1 mAh cm^{-2}, stripping to 1 V at 0.5 mA cm^{-2}, 2.5 mA cm^{-2} and 5.0 mA cm^{-2} (voltage profiles below 0 V represents the plating process, while those above 0 V represents the stripping process); (**b**) 2 M LiFSI–DMC, 0.5 M LiTFSI–DME/DOL, 1 M LiTFSI–DME/DOL, 1 M LiTFSI–DME/DOL + 2% $LiNO_3$, CCE + Cs^+ and CCE + FEC, plating at 0.5 mA cm^{-2} for 1 mAh cm^{-2}, stripping to 1 V at 0.5 mA cm^{-2}. **c**, The isolated metallic Li^0 percentage in total capacity loss ($Li^0/Li^0 + Li^+$). **d**, SEI Li^+ percentage in total capacity loss ($Li^+/Li^0 + Li^+$). **e**, Measured H_2 area as a function of Coulombic efficiency under a variety of testing conditions. Every data point is an average of three separate GC measurements. The error bars represent the standard deviation, indicating the accuracy and reproducibility of the GC measurement. **f**, Unit conversion between milliampere-hours and milligrams of Li.

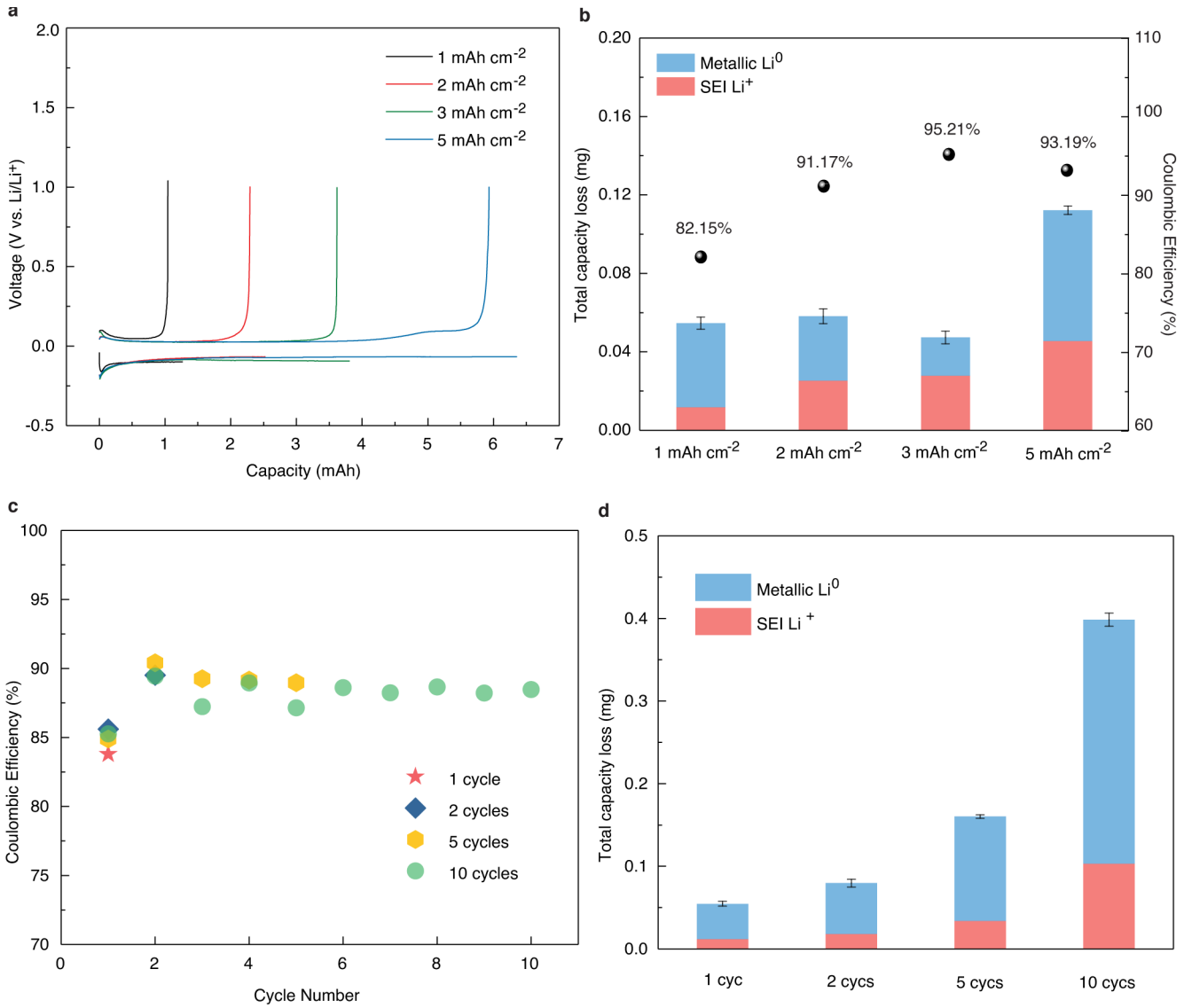

Extended Data Fig. 3 | TGC analysis of inactive Li formed under extended electrochemical conditions. a, The voltage profiles of CCE with different deposition capacities at 0.5 mA cm^{-2} for 1 mAh cm^{-2}, 2 mAh cm^{-2}, 3 mAh cm^{-2} and 5 mAh cm^{-2}. **b**, The corresponding TGC analysis of inactive Li with associated capacity loss and Coulombic efficiency under different deposition capacities. **c**, The cycling performance of CCE in Li||Cu half-cells at 0.5 mA cm^{-2} for 1 mAh cm^{-2}. **d**, TGC analysis showing Li^0 and Li^+ contents with associated capacity loss after one, two, five and ten cycles, respectively.

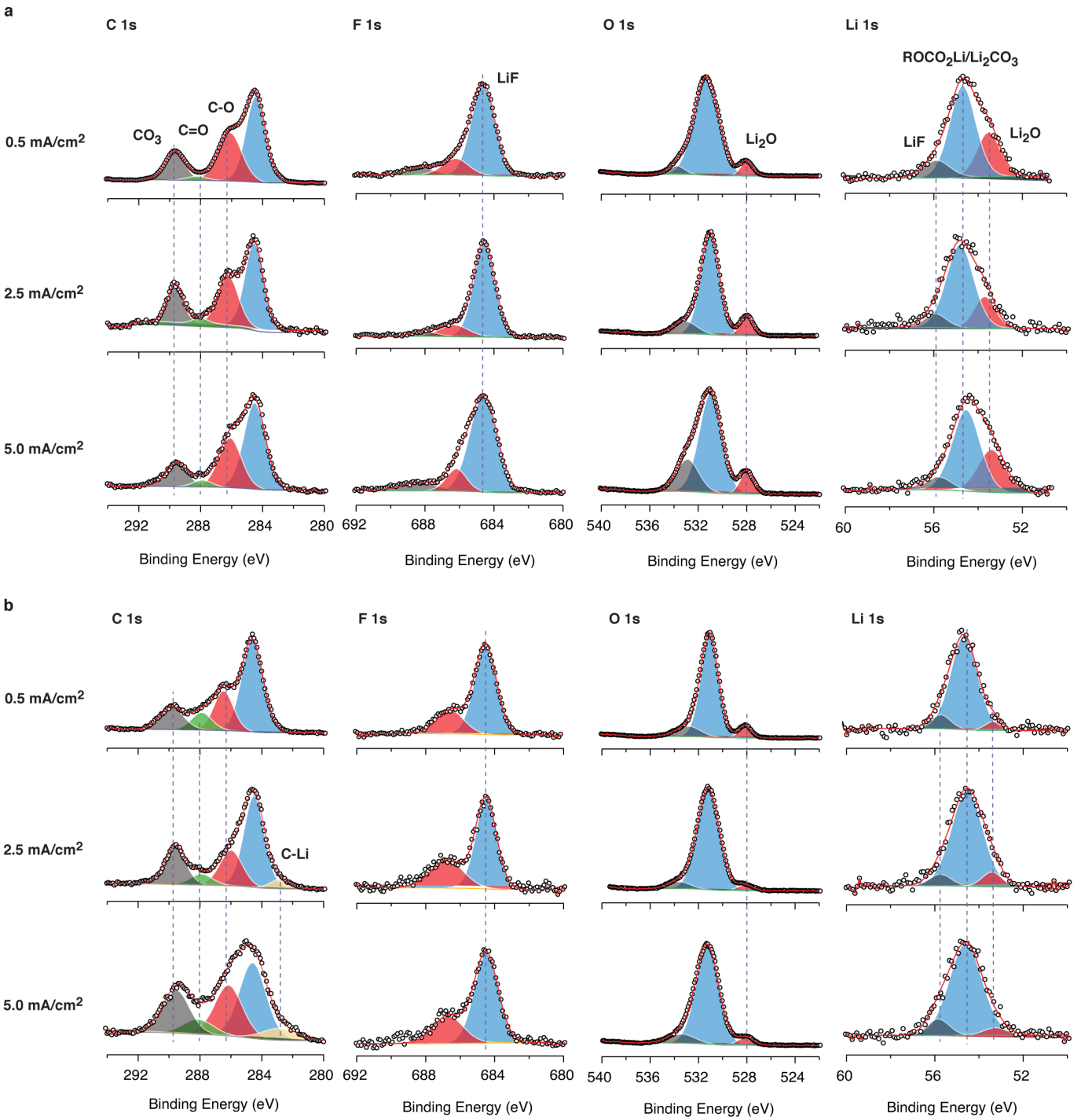

Extended Data Fig. 4 | XPS analysis of inactive Li SEI components formed in HCE and CCE for various stripping rates. a, Inactive Li formed in HCE. **b**, Inactive Li formed in CCE. The stripping rates show negligible impact on SEI components and contents in both electrolytes.

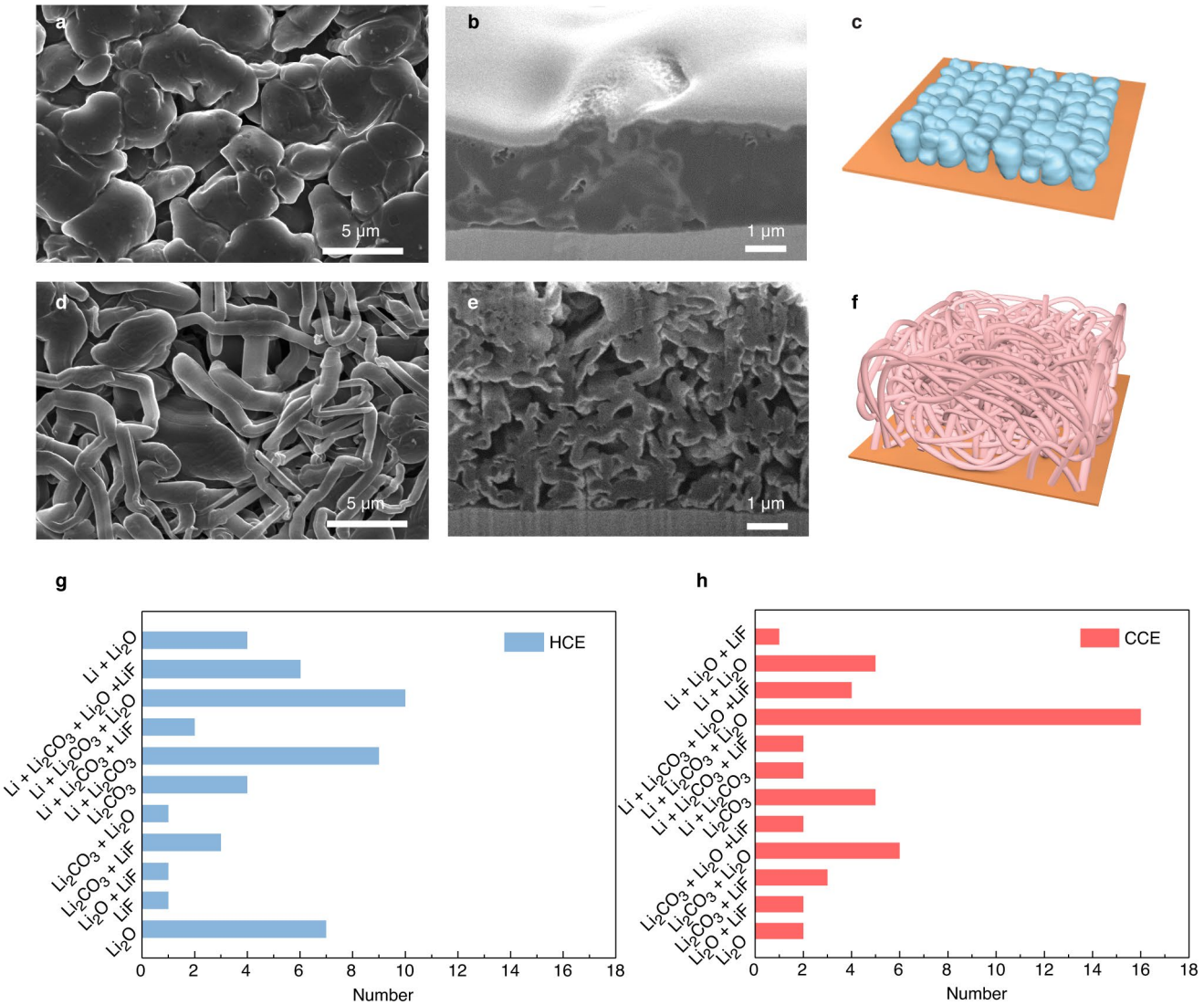

Extended Data Fig. 5 | Supplementary materials for cryo-FIB-SEM and cryo-TEM analysis. a–c, Top view, cryo-FIB cross-section and schematic of deposited Li in HCE, respectively. The Li deposited in HCE forms large particles with several micrometres in size, with reduced porosity. **d–f** Top view, cryo-FIB cross-section and schematic of deposited Li in CCE, respectively. The Li shows a whisker-like morphology with high porosity. All deposited at 0.5 mA cm^{-2} for 0.5 mAh cm^{-2}. **g**, Statistics of inactive Li SEI components formed in HCE, as detected at 50 different sample positions by cryo-TEM. **h**, Statistics of inactive Li SEI components formed in CCE, as detected at 50 different sample positions by cryo-TEM.

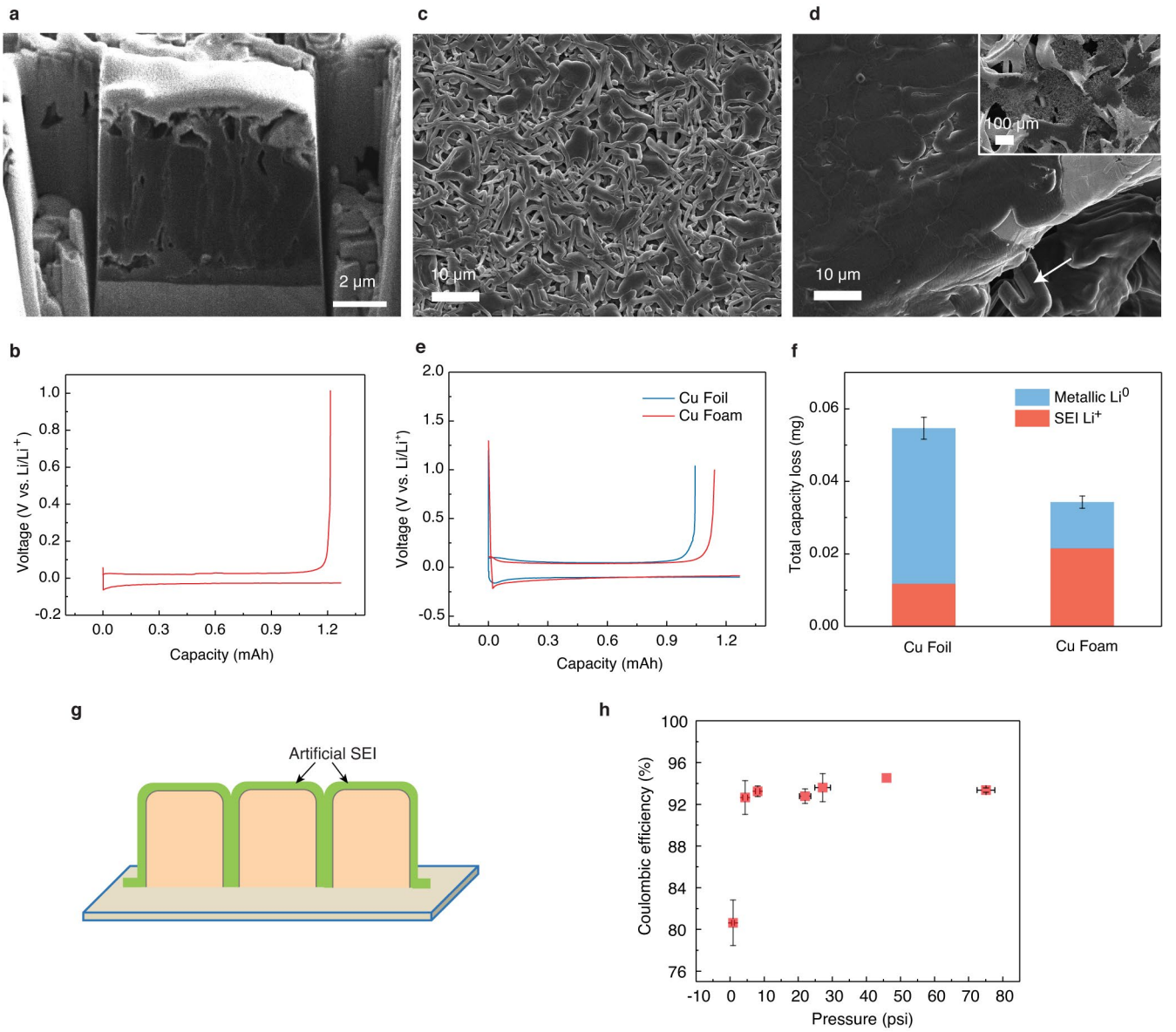

Extended Data Fig. 6 | Strategies that may mitigate inactive Li formation. a, Cross-sectional morphology of Li deposits generated in an advanced electrolyte developed by General Motors (GM), showing a columnar structure. **b**, The GM electrolyte delivers a first-cycle Coulombic efficiency of 96.2%, plating at 0.5 mA cm^{-2} for 1 mAh cm^{-2}, stripping at 0.5 mA cm^{-2} to 1 V. **c–f**, 3D current collector. **c**, SEM image of Li deposits on Cu foil. **d**, SEM image of Li deposits on Cu foam. Both were deposited at 0.5 mA cm^{-2} for 1 mAh cm^{-2} in CCE. **e**, Representative first-cycle voltage profiles of Cu foil and Cu foam, plating at 0.5 mA cm^{-2} for 1 mAh cm^{-2}, stripping at 0.5 mA cm^{-2} to 1 V in CCE. **f**, TGC quantification of inactive Li for Cu foil and Cu foam samples. **g**, Schematic of an ideal artificial SEI design. The polymer-based artificial SEI should be chemically stable against Li metal and mechanically elastic enough to accommodate the volume and shape change. Meanwhile, the edges of the artificial SEI should be fixed to the Li metal or the current collector, preventing the electrolyte from diffusing and making contact with fresh Li metal. The flexible polymer SEI thus can accommodate expansion and shrinkage during repeated Li plating and stripping. In this way, no Li will be consumed to form SEI during extended cycles, and we can realize anode-free Li metal batteries. **h**, Influence of pressure on Li plating/stripping. The results are from the HCE, at 0.5 mA cm^{-2} for 1 mAh cm^{-2}, using a load cell. At each condition, two load cells were measured. The error bars indicate the standard deviation.

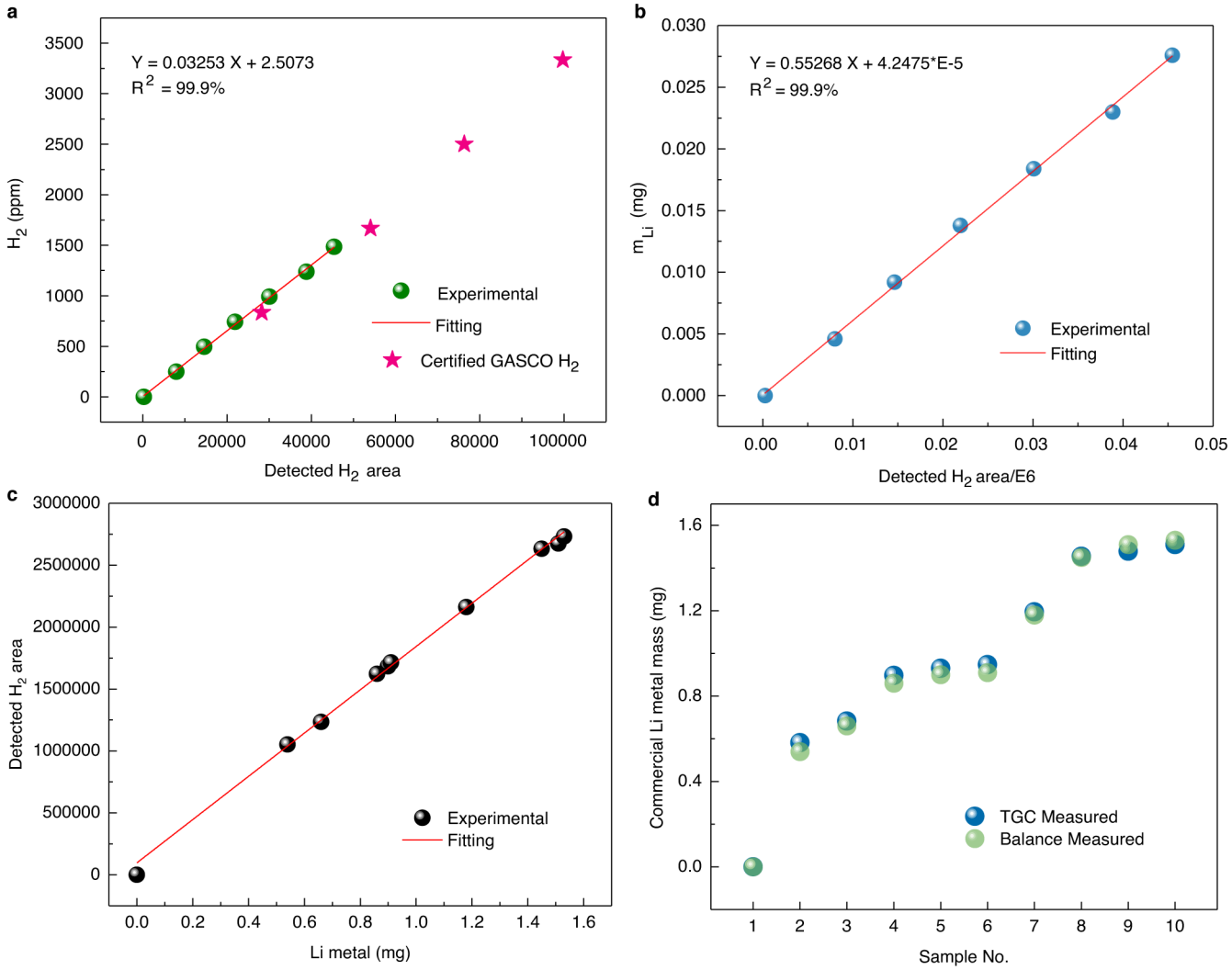

e

Li, mg	1	2	3	4	5	6	7	8	9	10
TGC	0.0005	0.5820	0.6825	0.8970	0.9304	0.9472	1.1943	1.4550	1.4781	1.5098
Balance	Blank	0.54	0.66	0.86	0.90	0.91	1.18	1.45	1.51	1.53

Significant digits of the measurement methods are marked in red.

f

Blank Sample Trial No.	1	2	3	4	5	6	7	8	9	10
H_2 concentration in ppm	47.20	58.27	54.39	41.07	46.54	51.02	51.03	54.65	45.49	53.98

Extended Data Fig. 7 | TGC calibration and LOD/LOQ analysis. a, H_2 concentration in ppm calibration curve as a function of detected H_2 area and verification with certified GSCO H_2 calibration gas. **b**, Converted metallic Li^0 mass calibration curve as a function of detected H_2 area. **c**, Nine pieces of Li metal with known mass were tested using the TGC set-up. The strongly linear relationship with detected H_2 area indicates the feasibility of this method. **d**, Comparison between the balance-measured mass and TGC-quantified mass of the commercial Li metal pieces. **e**, Numerical comparison between the balance-measured mass and TGC-quantified mass of the commercial Li metal pieces. As the accuracy of the balance is two orders of magnitude lower than the TGC (10^{-5} g versus 10^{-7} g), the differentials should mainly come from the balance. **f**, H_2 concentration in the blank samples measured for LOD/LOQ analysis. A total of 10 measurements were taken for the LOD/LOQ calculation.

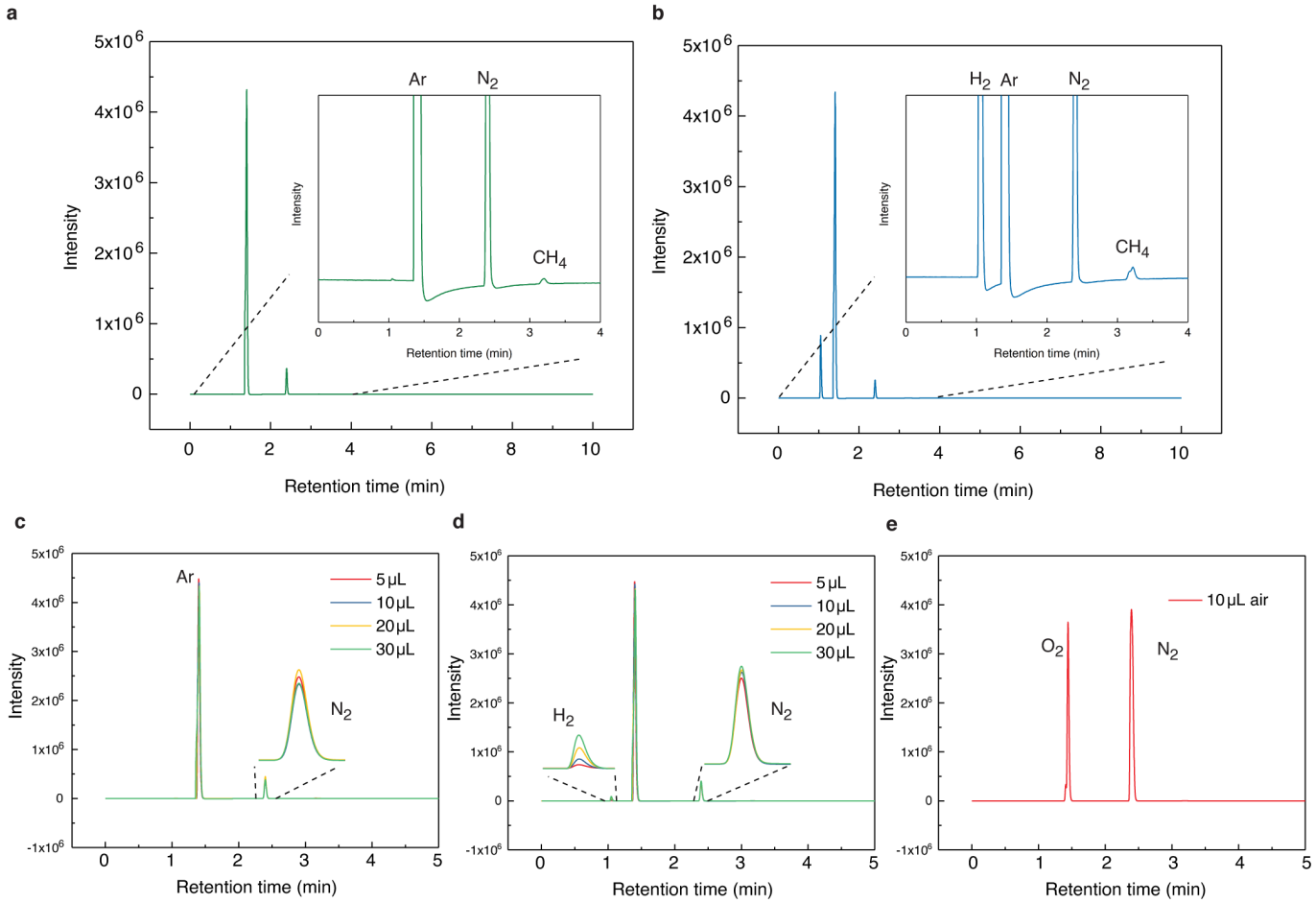

Extended Data Fig. 8 | GC chromatogram and N_2 interference analysis. a, GC chromatogram of the background gas from glovebox. **b**, GC chromatogram of gases with H_2 after H_2O titration on metallic Li^0. **c**, Glovebox background gas measurements with various sampling amounts. The N_2 amounts remain at the same level with various injection amounts, indicating the N_2 does not exist in the reaction container. **d**, Container gas measurements with various sampling amounts after the H_2O titration. The N_2 amounts still remain identical with different injection amounts, whereas the H_2 amounts increase in proportion to the increment of injection amounts, indicating that the N_2 does not originally exist in the reaction container but comes from the gas sampling process, and thus will not have any chemical reactions with the inactive Li samples; the H_2 quantification is not influenced by the injection sampling process. **e**, GC chromatogram of 10 μl of air.

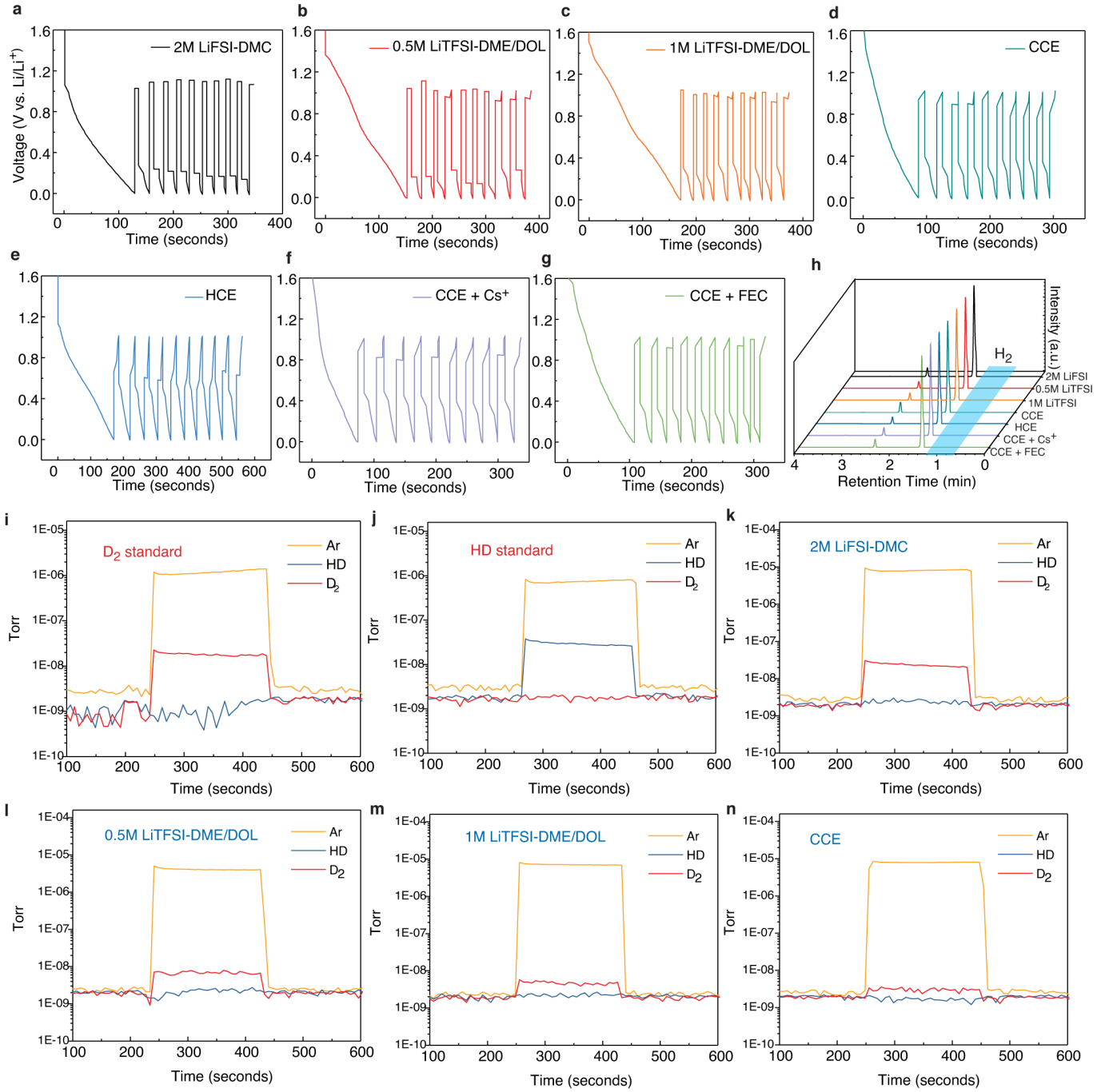

Extended Data Fig. 9 | Analysis of possible LiH presence in inactive Li. a-h, Possible influence from LiH in SEI. **a–g**, The voltage profiles of SEI formation between 0 V and 1 V at 0.1 mA for ten cycles in 2 M LiFSI–DMC (**a**), 0.5 M LiTFSI–DME/DOL (**b**), 1 M LiTFSI–DME/DOL (**c**), CCE (**d**), HCE (**e**), CCE + Cs^+ (**f**) and CCE + FEC (**g**). After the SEI formation, we performed TGC measurements on the current collectors with SEI. **h**, TGC results of the seven types of electrolytes. No H_2 can be detected from any of them, indicating no LiH presence in the SEI of the systems studied. **i–n**, Possible influence from LiH in bulk inactive Li. To differentiate the two species, we substitute the titration solution with D_2O instead of H_2O. The D_2O reacts with LiH and metallic Li^0 to produce HD and D_2, respectively. RGA can effectively distinguish between HD (relative molecular mass 3) and D_2 (relative molecular mass 4) by partial pressure analysis. **i**, The D_2 standard from the reaction between commercial pure Li metal and D_2O. **j**, The HD standard from the reaction between commercial LiH powder and D_2O. **k–n**, Analysis of gaseous products from reactions between D_2O and inactive Li forming in 2 M LiFSI–DMC (**k**), 0.5 M LiTFSI–DME/DOL (**l**), 1 M LiTFSI–DME/DOL (**m**) and CCE (**n**).

Extended Data Table 1 | The solubility or reactivity of known SEI species with H_2O

SEI component	Solubility in 100 mL H_2O
LiF	0.134 g (0.67 mg in 0.5 mL H_2O)
LiOH	12.8 g
$Li_2C_2O_4$	8 g
Li_2CO_3	1.29 g
Li_2O	$Li_2O + H_2O = 2LiOH$
CH_3Li	$CH_3Li + H_2O = LiOH + CH_4 \uparrow$
ROLi	$ROLi + H_2O = LiOH + ROH$
$(CH_2OCO_2Li)_2$	$(CH_2OCO_2Li)_2 + H_2O = Li_2CO_3 + (CH_2OH)_2 + CO_2 \uparrow$
$LiOCO_2R$	$2LiOCO_2R + H_2O = Li_2CO_3 + 2ROH + CO_2 \uparrow$